

Impact of Nanoscopic Impurity Aggregates on Cavitation in Water

Marin Šako,^{†,‡} Roland R. Netz,[¶] and Matej Kanduč^{*,†}

[†]Jožef Stefan Institute, Jamova 39, 1000 Ljubljana, Slovenia

[‡]Faculty of Mathematics and Physics, University of Ljubljana, Jadranska 19, 1000 Ljubljana, Slovenia

[¶]Fachbereich Physik, Freie Universität Berlin, Berlin 14195, Germany

E-mail: matej.kanduc@ijs.si

Abstract

The stability of water against cavitation under negative pressures is a phenomenon known for considerable discrepancies between theoretical predictions and experimental observations. Using a combination of molecular dynamics simulations and classical nucleation theory, we explore how nanoscopic hydrocarbon droplets influence cavitation in water. Our findings reveal that while a macroscopic volume of absolutely pure water withstands up to -120 MPa of tension, introducing a single nanoscopic oil droplet, merely a few nanometers in radius, brings this cavitation threshold to around -30 MPa, closely matching the values typically observed in highly controlled experiments. The unavoidable presence of nanoscopic hydrophobic impurities, even in highly purified water used in experiments, imposes a practical limit on achieving the theoretical tensile strength in realistic settings. More broadly, our study highlights the profound impact of nonpolar residues on nucleation phenomena and enhances our understanding of metastability in real-world systems.

KEYWORDS: *cavitation, bubble, droplet, water, oil, molecular dynamics simulation*

1. INTRODUCTION

Liquids can be brought into a metastable state relative to their vapor in two ways: either by superheating them beyond their boiling temperature or by stretching them below their saturated vapor pressure. Eventually, they will revert to equilibrium through the nucleation of vapor bubbles, a phenomenon known as cavitation. The ability of a liquid to withstand mechanical tension and maintain negative pressures highlights the cohesive forces among its molecules. Water is a paradigmatic example, owing to its exceptional cohesion due to hydrogen bonds.¹

The phenomenon of negative pressures in liquids may seem counterintuitive at first, yet it commonly occurs in nature. A famous example is the sap in plants, reaching negative pressures as deep as -10 MPa,² which helps it to ascent against gravity. Octopuses and squids utilize negative pressures in their suckers for effective adhesion,³ whereas ferns exploit negative pressure for spore dispersal through a catapult-like mechanism.⁴ In porous media, soil, and microfluidic capillaries, water can experience tension because of curved air–water interfaces or evaporation.^{5–7} When cavitation bubbles form under tension, they collapse violently when the tension is released, generating microjets and shock waves, which can damage nearby surfaces, causing erosion in turbomachinery or harm biological tissues.^{8–11} Conversely, cavitation is the basis of lithotripsy, a medical procedure that uses acoustic shock waves to break down kidney stones and other calcifications within the body, the exact mechanism of which is still debated.^{1,12}

The study of water under tension and cavitation, dating back to the 17th century,¹ has inspired researchers to understand not only the metastable phase diagram of water and its thermodynamic anomalies, but also shed light on the nature of first-order transitions as

a fundamental phenomenon.¹³ Cavitation inception, a key process in this scope, is the stochastic nucleation of a vapor bubble. The interplay between the volume and surface energies of the bubble creates an energy barrier that has to be surmounted by the thermal fluctuations within the system. This concept forms the cornerstone of Classical Nucleation Theory (CNT),¹⁴ which suggests that water at room temperature should sustain negative pressures between about -120 and -160 MPa for extended periods of time.^{1,15–18} This remarkably high degree of metastability has been confirmed also by recent computer simulation studies.^{19–22}

However, in less controlled experiments, cavitation in water occurs near saturated vapor pressure (around 2 kPa), preventing it from reaching a significantly metastable state. The prevalent understanding is that cavitation initiates at the weak points within a liquid, such as hydrophobic surfaces, impurities, and especially pre-existing bubbles,^{23–25} as demonstrated by systematic experiments²⁶ and simulations.²⁷ Indeed, purifying and degassing water enhances its sustainability against tension and allows it to withstand considerable negative pressures. However, even the most rigorous purification methods combined with acoustic cavitation or shock waves techniques that avoid solid boundaries seem to consistently reach a threshold of only about -30 MPa,^{1,13,17,28} which is by a factor of 4–5 below theoretically predicted values. A notable exception involves micro-sized inclusions in minerals, similar to the Berthelot tube method,^{18,29,30} where negative pressures up to -140 MPa can be achieved, though the reasons for this are not fully understood.

A prevailing hypothesis attributes the gap between theory and experiment to nanoscale nuclei suspended even in highly purified water, as achieving absolute purity in large liquid volumes is practically impossible.^{27,31–33} Indeed, recent MD simulations indicate that solid particles can promote cavitation within simulation volumes by dis-

rupting the hydrogen-bond network.³⁴ Nevertheless, it remains uncertain whether such trace contaminants meaningfully contribute to the cavitation of macroscopic systems, given that their minute amounts may have a limited influence on the entire system. While testing this “contamination hypothesis” via experiment is very challenging, theoretical approaches offer a vital alternative.

In this study, we quantify the influence of nanoscale impurities, specifically hydrophobic oil droplets, on the cavitation pressure of water. Using MD simulations combined with CNT, we demonstrate that a single nanoscopic oil droplet, only a few nanometers in radius, suspended in a large volume of water brings the cavitation threshold to around -30 MPa, closely matching experimental observations. These results represent the first quantitative perspective into how non-soluble nanoscale impurities set the reported practical limit on water’s tensile strength in realistic environments, thereby helping to bridge the gap between theory and experiment. Our simulations provide insights into cavitation inception at hydrophobic droplets, relevant to applications such as ultrasonic emulsification. They clarify how hydrophobic inclusions influence cavitation thresholds in water, offer an explanation for why the theoretical limit is reached only in microscale systems, and shed light on mechanisms of cavitation resilience in plant sap.

2. RESULTS AND DISCUSSIONS

2.1. Homogeneous cavitation in absolutely pure water. CNT is foundational in the study of homogeneous cavitation, offering a framework to understand the transition from a metastable to a stable phase in liquids.^{1,18,19} CNT posits that cavitation inception occurs with the stochastic formation of a bubble within the bulk liquid, which occurs under substantial negative pressures. The free energy of an expanding spherical cavity of radius r under negative pressure p is expressed as

$$G_w(r) = 4\pi\gamma(r)r^2 + \frac{4}{3}\pi pr^3 \quad (1)$$

where the first term is associated with the free energy of creating the bubble interface and the second term to the work gained by performing the volume expansion against the ambient pressure. Achieving accurate quantitative agreement with molecular simulations requires considering the impact of interface curvature on surface tension, $\gamma(r)$, as highlighted before.^{19,35} We describe the curvature-dependent surface tension as $\gamma(r) = \gamma_w(1 + 2\delta_w/r)$, where γ_w is the surface tension of the flat water–vapor interface and δ_w the Tolman length. The Tolman length quantifies the deviation in surface tension between a curved and a planar interface, which becomes significant for nanometer-scale radii. This expression represents the first-order Taylor expansion of Tolman’s original expression,³⁶ which is applicable in scenarios of small curvatures ($r \gg |\delta_w|$). Equation 1 neglects the effect of vapor inside the cavity, which is reasonable given that the typical cavitation pressures are much higher in magnitude (tens of MPa) than the saturated vapor pressure at room temperature (several kPa).

The competition between the two terms in eq 1, each of a different sign (note that $p < 0$) and scaling differently with the bubble radius, results in a free energy maximum G_w^* at the critical radius r^* . To first-order in δ_w , the critical radius, determined by the condition $dG_w/dr = 0$, expresses as

$$r^* = -\frac{2\gamma_w}{p} + \delta_w \quad (2)$$

and the free energy barrier as

$$G_w^* = \frac{16\pi\gamma_w^3}{3p^2} - \frac{16\pi\gamma_w^2\delta_w}{p} \quad (3)$$

A bubble exceeding the radius r^* will spontaneously grow, leading to a spread over the entire system.

Cavitation is a thermally activated stochastic process in which a bubble in a given volume spontaneously reaches the critical size. According to reaction rate theory, the rate of cavitation within this volume is given by^{35,37}

$$k_w = \kappa_w V_w e^{-\beta G_w^*} \quad (4)$$

Here, the kinetic prefactor $\kappa_w V_w$ denotes the frequency of cavitation attempts, which is proportional to the volume of the liquid V_w . The quantity κ_w is the attempt frequency density, an intensive property of the liquid. The Boltzmann factor, $\exp(-\beta G_w^*)$, accounts for the probability that an individual attempt reaches the critical size.

The survival probability that the system has not yet cavitated decays exponentially with time as $\exp(-k_w t)$. Thus, the cavitation rate k_w represents the inverse of the mean time for cavitation to occur, $\tau = k_w^{-1}$. In practical terms, it is often more useful to discuss cavitation in the context of cavitation pressures rather than cavitation times. Specifically, we define the cavitation pressure p_{cav} as the pressure at which the likelihood of cavitation reaches e^{-1} for a given time τ . Note that an alternative definition of the cavitation pressure, at which the probability reaches 1/2 is also used in the literature,¹ leading to a negligible difference in cavitation pressure. From the expressions for the free energy barrier (eq 3) and cavitation rate (eq 4) and considering the result for the mean cavitation time $\tau = k_w^{-1}$, we can compute the cavitation pressure. If we disregard the curvature dependence of surface tension (i.e., setting $\delta_w = 0$), as traditionally done in the literature, we get the following, well-established CNT prediction for the cavitation pressure^{1,38}

$$p_{cav}^{(0)} = -\sqrt{\frac{16\pi\gamma_w^3}{3k_B T \ln(\kappa_w V_w \tau)}} \quad (5)$$

where τ is considered as the observation time. Incorporating the first-order curvature correction, results in the following modified expression for the cavitation pressure

$$p_{cav} = p_{cav}^{(0)} \left(1 - \frac{3\delta_w}{2\gamma_w} p_{cav}^{(0)} \right) \quad (6)$$

This modified expression is accurate when the second term in parentheses is much less than 1, a condition met in our system.

Determining the attempt frequency density, κ_w , and the Tolman length, δ_w , presents a considerable challenge, as they are not amenable to simple continuum descriptions. Instead, these parameters require molecular-level considerations for an accurate estimation. While various theoretical estimates exist for the attempt frequency,^{39,40} their reliability often remains questionable. Fortunately, advancements in molecular simulations provide a robust solution to this challenge, offering detailed microscopic insights into cavitation and enabling precise quantification of relevant physical quantities.^{19,35,41}

When simulating cavitation, it is essential that the model accurately reproduces surface tensions. After evaluating four popular water models, we selected TIP4P/2005,⁴² which has a surface tension of 68 mN/m, closely matching the experimental value. In our simulations, we employ the pressure-ramp technique,^{35,43} where the negative pressure decreases linearly over time, as outlined in the Methods

section. In this approach, cavitation (an example of which is shown in Figure 1a) occurs at a dynamic cavitation pressure dependent on the applied pressure rate. From the relationship between dynamic cavitation pressures and pressure rate (Figure 5a in the Methods section), we derive two key parameters: the Tolman length ($\delta_w = -0.058$ nm) and the attempt frequency density ($\kappa_w = 1.25 \times 10^{18}$ s $^{-1}$ nm $^{-3}$).

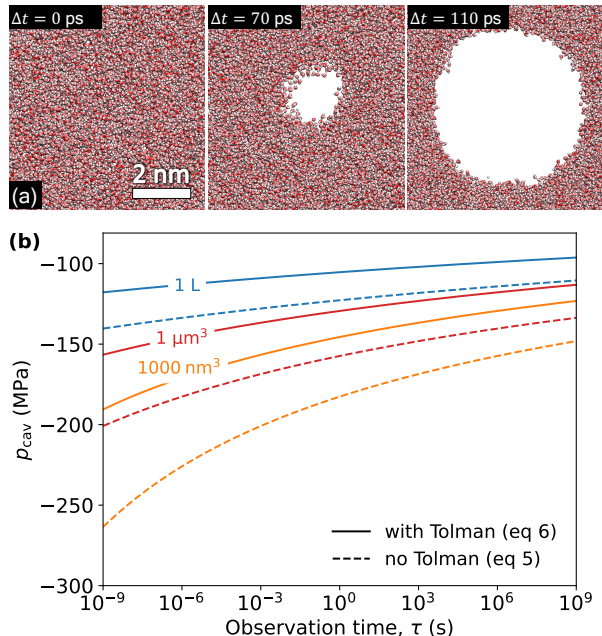


Figure 1: (a) Sequential snapshots of a cavitation event in absolutely pure bulk water from a pressure-ramp simulation, occurring as the ramping pressure reached $p_{cav}^* = -178$ MPa under an imposed pressure rate of $\dot{p} = -1$ MPa ns $^{-1}$. Each snapshot shows a thin cross-sectional slab through the cavitation site. The values of Δt indicate the elapsed time from a reference point just at cavitation onset. (b) Cavitation pressure as a function of observation time for three different volumes of bulk TIP4P/2005 water. Dashed lines show the result without the Tolman correction (eq 5), and the full lines are the results with the Tolman correction (eq 6).

These parameters were then used in the CNT model (5 and eq 6) to calculate the cavitation pressures for variable volumes at static conditions. Figure 1b shows these pressures for three different volumes of absolutely pure water against observation time (solid lines). Longer observation times and larger volumes result in slightly less negative cavitation pressures. However, their influence is very weak, as they combine within the logarithmic function under the square root in eq 5. For a wide range of practical scenarios, ranging from microseconds to years ($\sim 10^8$ s) and involving water volumes from cubic micrometers to liters, cavitation pressures span between -100 and -150 MPa. This relatively narrow window allows us to consider the cavitation pressure, in a rough approximation, as the tensile strength of water in the sense of an intrinsic material property. Additionally, for typical simulation volumes of $10 \times 10 \times 10$ nm 3 (solid orange line), the cavitation pressures are around -190 MPa, close to the dynamic cavitation pressures in our pressure-ramp simulations (Figure 5a in the Methods section).

The negative Tolman length in our water model reduces the critical bubble radius (eq 2) and lowers the free energy barrier (eq 3), which facilitates cavitation. For comparison, we also show predictions

without the Tolman correction (eq 5), represented by dashed lines in Figure 1b, consistent with other theoretical studies.^{1,15-18} These values are about 20% higher in magnitude than those with the correction. Although often disregarded in CNT models to avoid complexity, the Tolman correction significantly impacts results, highlighting the importance of accounting for curvature-dependent surface tension for accurate quantitative predictions.

It is important to recognize that the outcomes of simulations are influenced by the choice of the water model. For reference, we conducted additional simulations using the OPC water model,⁴⁴ known for its very accurate reproduction of the surface tension of actual water, yielding $\gamma_w = 72$ mN/m. As expected, the OPC model results in slightly more negative cavitation pressure values. However, the difference is relatively minor, amounting to only a few percent. This small variance underscores the robustness of the conclusion that ideally clean water cavitates at pressures between -100 and -150 MPa, in agreement with other theoretical predictions.^{1,15-18}

Yet, a persistent question is why most carefully conducted experiments with ultra-purified water (purified and degassed as much as possible) consistently report cavitation pressures that are 4 to 5 times lower than the theoretical value.^{1,13,17} The harsh reality is that achieving absolute purity in liquids is virtually impossible, as trace impurities are almost always present.^{31,32} Notably, even the highest grade of ultrapure water achievable with current technology still contains total organic carbon (TOC) levels above 1 $\mu\text{g/L}$.^{33,45} In a cubic millimeter of such water, the entire organic matter is equivalent in volume to a droplet of about 1 μm in diameter. While smaller and medium-sized organic molecules may dissolve, larger molecules, such as typical phospholipids⁴⁶ or alkanes with more than 12 carbon atoms⁴⁷ have solubilities comparable or below this TOC level and thus tend to stay aggregated. Consequently, hydrocarbon aggregates are inevitably present in any macroscopic volume of water, even when it is highly purified.⁴⁸ This notion brings us to an important question: could these tiny aggregates—referred to here as droplets—even in minimal quantities, impact the tensile strength of the entire aqueous system? Addressing this question is the central aim of the remaining part of our study.

2.2. Homogeneous cavitation in bulk liquid hydrocarbon.

Before delving into the impact of small hydrophobic droplets, we first analyze homogeneous cavitation in a pure liquid hydrocarbon subjected to negative pressure. This setup effectively represents cavitation inside a large oil droplet, as the expansion of the outer droplet boundary becomes negligible before the nucleating bubble inside the droplet reaches the critical size. Consequently, the expressions for the cavitation pressure in this scenario are equivalent to that of bulk water (eqs 5 and 6) with appropriate substitutions of the quantities to account for the properties of the oil, specifically, $\gamma_w \rightarrow \gamma_o$, $\delta_w \rightarrow \delta_o$, and $\kappa_w \rightarrow \kappa_o$. To derive these parameters, we extended our simulation to include bulk decane, conducting them in an analogous way as performed with bulk water. We employed the CHARMM36 force field for decane, which accurately reproduces decane–vapor⁴⁹ and decane–water surface tensions. Pressure-ramp simulations of bulk decane (results shown in Figure 5b in the Methods section) provided the values for κ_o and δ_o listed in Table 1.

The cavitation pressures for bulk decane based on eqs 5 and 6 behave qualitatively similar to those for water, but fall within the range of -20 to -30 MPa for volumes ranging from cubic micrometers to liters and observation times from microseconds to days. This range is consistent with measured cavitation pressures in many other organic liquids.⁵⁰⁻⁵³ The reduced threshold in hydrocarbons arises primarily from their lower surface tension values, $\gamma_o \approx 20$ – 30 mN/m,

which are comparable across most organic liquids⁵⁴ and significantly lower than that of water. The surface tension of hydrocarbons is primarily due to weak cohesive forces driven by dispersion (London) interactions, whereas the high surface tension of water and corresponding strong cohesion are due to hydrogen bonding. Overall, the cavitation pressure in hydrocarbons is roughly five times lower in magnitude than that of bulk water. This difference can be expressed analytically from eq 5 for water and oil parameters in the macroscopic limit, where $Vt \rightarrow \infty$, and one indeed finds $p_{\text{cav,o}}/p_{\text{cav,w}} \approx (\gamma_o/\gamma_w)^{3/2} \approx 1/5$. Thus, the disparity in tensile strengths between water and hydrocarbon is primarily influenced by the different surface tensions of the two liquids.

2.3. Cavitation of water containing oil nanodroplets. An intriguing question is whether nonsoluble hydrocarbons also influence cavitation when present as nanoscopic droplets in water. To investigate this, we proceed by considering a macroscopically large volume of water, V_w , containing a single oil droplet of radius R_o , as illustrated in Figure 2a. We then extend our analysis to a system with N monodisperse oil droplets.

Under negative pressures, this system can undergo three generic cavitation scenarios: The bubble can nucleate (i) in the bulk water phase (Figure 2b), (ii) at the droplet–water interface (Figure 2c), or (iii) inside the oil droplet (Figure 2d).

These three scenarios represent three distinct pathways for the cavitation process within the system. Each pathway evolves with its specific rate, and the overall cavitation rate of the system is the sum of all the contributions, assuming they proceed independently. For generality, we express the overall cavitation rate for a system with N monodisperse oil droplets as

$$k = k_w + Nk_{\text{ow}} + Nk_o \quad (7)$$

The first pathway, homogeneous cavitation within the bulk water phase, is characterized by the cavitation rate k_w and is given by eq 4. Moving on to cavitation in the droplet’s interior (Figure 2d), the cavitation rate for a single droplet can be expressed as

$$k_o = \kappa_o V_o e^{-\beta G_o^*} \quad (8)$$

where κ_o is the attempt frequency per volume of oil, derived from our bulk decane simulations in the previous section, $V_o = (4\pi/3)R_o^3$ is the volume of the oil droplet, and G_o^* is the corresponding free energy barrier. The latter is the maximum in the free energy of a bubble nucleating within the droplet, which we formulate as

$$G_o(r) = 4\pi\gamma_o(1 + 2\delta_o/r)r^2 + 4\pi\gamma_{\text{ow}} [R(r)^2 - R_o^2] + \frac{4}{3}\pi pr^3 \quad (9)$$

and is associated with the expansion of two interfaces: the inner one of radius r , characterized by the oil–vapor surface tension γ_o , and the outer interface of radius R , characterized by the oil–water surface tension γ_{ow} . The two radii are linked through the reasonable assumption that the oil volume remains constant, leading to $R^3 = R_o^3 + r^3$. In the above expression, we have only included the term associated with the curvature correction of the inner oil–vapor interface (described by the Tolman length γ_o). We have omitted the curvature correction of the outer oil–water interface, reading $8\pi\gamma_{\text{ow}}\delta_{\text{ow}}(R - R_o)$, where δ_{ow} is the Tolman length of the oil–water interface, which we have not quantified. This omission is justifiable, especially for larger droplets where R_o significantly exceeds r . In such cases, we can approximate $R - R_o \approx r^3/(3R_o^2)$,

resulting in a much smaller contribution from the curvature correction of the oil–water interface compared to the curvature correction of the internal, oil–vapor interface. The maximum in $G_o(r)$ does not lend itself to a simple analytical expression and requires numerical evaluation.

Finally, the rate of heterogeneous cavitation at the oil–water interface of a single droplet (Figure 2c) is governed by the equation

$$k_{\text{ow}} = \kappa_{\text{ow}} A_o e^{-\beta G_{\text{ow}}^*} \quad (10)$$

where κ_{ow} represents the cavitation attempt frequency per surface area of the droplet, $A_o = 4\pi R_o^2$ is the droplet’s surface area, and G_{ow}^* is the associated free energy barrier.

To quantify this cavitation pathway, we performed a series of simulations with decane droplets with radii ranging from 2.5 to 6.5 nm. Density and order-parameter profiles indicated a rapid transition to an isotropic bulk-like region inside the droplet, with an effective water–decane interface being approximately half a nanometer thick. Exposing these droplets to increasing negative pressures, we consistently found that cavitation begins at the oil–water interface, thus, corresponding to the heterogeneous cavitation scenario. An example of such cavitation is captured by sequential snapshots in Figure 3 for a droplet with an initial radius of 4.2 nm.

Heterogeneous nucleation at the droplet interface involves three phases in direct contact, resulting in a more complex geometry than in the other two pathways. Because the shapes do not conform to equilibrium geometries,⁵⁵ formulating an expression for G_{ow}^* becomes challenging. As seen from the snapshots, the nucleating cavity expands predominantly into the oil phase, while the water phase retains a nearly spherical interface with both the oil and the vapor. Conceptually, this scenario can be envisioned as bringing a spherical bubble from the droplet’s interior to its outer interface with water, creating a water–vapor interface while eliminating the oil-bound interfaces at the patch. Antonov’s rule states that the interfacial tension between two liquids approximately equals the difference in their respective surface tensions with vapor, that is, $\gamma_o + \gamma_{\text{ow}} \approx \gamma_w$.⁵⁶ This relation implies that the transition of a spherical bubble results in minimal net change in free energy.

Thus, the distinction between G_{ow} and G_o arises primarily from additional correction terms in the former, such as the Tolman curvature corrections of the water–vapor interface and the contribution of the three-phase contact line where oil, water, and vapor meet. Quantifying these contributions is challenging. Since all these factors scale linearly with the bubble radius, r , we adopt the expression for the free energy as given by eq 9 but substitute the oil–vapor Tolman length with an effective value, thus $G_{\text{ow}} = G_o(\delta_o \rightarrow \delta_{\text{eff}})$. This “effective Tolman length” serves as a fitting parameter to our simulation results, offering a pragmatic approach to encompass these complexities. Performing pressure ramp simulations and fitting their results (shown in Figure 5c in the Methods section) yield the parameters κ_{ow} and δ_{eff} , listed in Table 1. We note that the global fit is not perfect, likely reflecting the complexity and dynamic nature of the cavitation geometry. A better fit would require higher-order corrections in the free energy or even in the attempt frequency density, which, however, is beyond the scope of this study.

Equipped with all the required model parameters, we are now set to calculate the cavitation pressure by solving eq 7. Unlike the scenario of cavitation in bulk liquid, where an analytical expression was possible (provided by eqs 5 and 6), we have to rely on numerical methods in this case. Doing so, we plot the calculated cavitation pressure for $V_w = 1$ liter of water containing a single decane droplet ($N = 1$) as a function of its radius R_o for three observation times in Figure 4. This plot represents the central finding of our study.

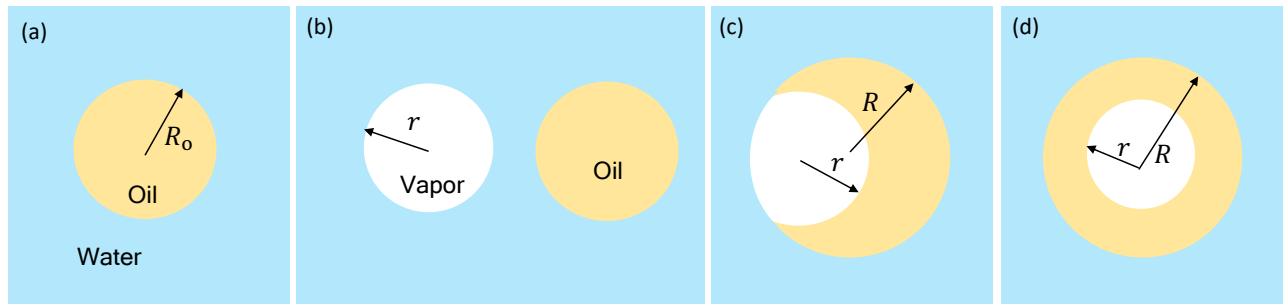


Figure 2: (a) Oil droplet of initial radius R_o in water can undergo three cavitation scenarios: (b) homogeneous cavitation inside the bulk water phase, (c) heterogeneous cavitation at the droplet interface, and (d) cavitation inside the oil droplet.

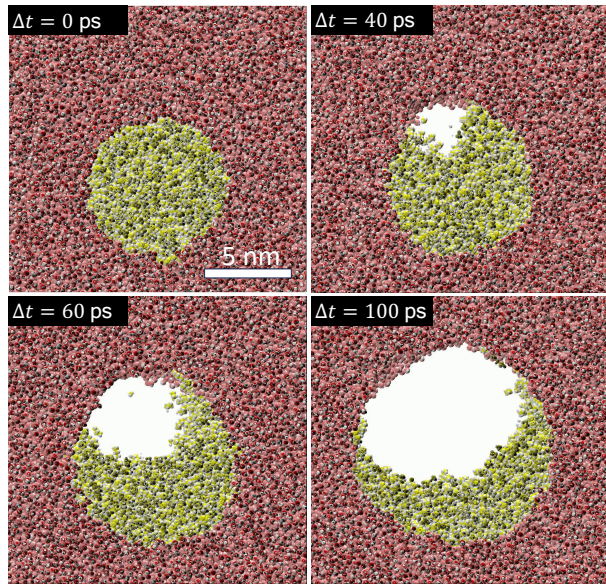


Figure 3: Sequential snapshots from a pressure-ramp simulation at a rate of $\dot{p} = -1 \text{ MPa ns}^{-1}$, showing a cavitation event of a decane droplet with an initial radius of $R_o = 4.2 \text{ nm}$ in water. The cavitation occurred as the pressure decreased to $p_{cav}^* = -63 \text{ MPa}$. Each snapshot represents a thin cross-sectional slab through the droplet center.

In the case of a vanishing droplet, $R_o \lesssim 1 \text{ nm}$ [region (i)], the cavitation rate is dominated by the first term in eq 7 (homogeneous cavitation in water), and the cavitation pressure of the system converges to the tensile strength of absolutely pure water, as given by eq 6. A notable transition occurs when the droplet radius exceeds approximately 1.5 nm. At this point, the cavitation pressure abruptly increases to less negative values [region (ii)]. This transition occurs when the rate of heterogeneous cavitation reaches that of the bulk water phase, $k_w = k_{ow}$ (denoted by the left vertical dotted line). The total volume of the system, V_w , has a minor effect on this transition. As the droplet radius continues to increase, the predominant cavitation mechanism transitions from heterogeneous to in-droplet cavitation [region (iii)]. The crossover between the two pathways, i.e., when their rates are equal, i.e., $k_{ow} = k_o$, occurs at a droplet radius of approximately 80 nm (denoted by the right vertical dotted line). Beyond this size, bubble nucleation primarily occurs within the hydrocarbon phase of the droplets.

Two key insights emerge from Figure 4. The first and most important

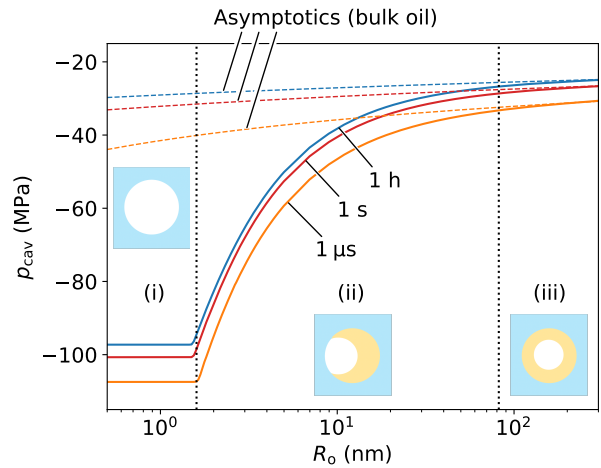


Figure 4: Cavitation pressure (tensile strength) of 1 liter of water containing a single decane droplet ($N = 1$) plotted versus its radius for various observation times τ (solid lines). With an increasing droplet size, the cavitation starts as homogeneous cavitation in bulk water [region (i)], crosses over at $R_o \approx 1.5 \text{ nm}$ to heterogeneous cavitation at the droplet surface [region (ii)], and at $R_o \approx 80 \text{ nm}$ eventually crosses over to cavitation in the droplet's interior [region (iii)]. For large droplets, the cavitation pressures asymptotically approach the results for bulk decane of equivalent volume (shown by dashed lines).

insight is that remarkably tiny amounts of nonpolar material are sufficient to substantially reduce the cavitation pressure of an entire macroscopic aqueous system. A single oil nanodroplet, only a few nanometers in size, weakens the tensile strength from the theoretical value for absolutely pure bulk water (around -100 MPa for 1 liter) down to the tensile strength typical of hydrocarbons, which is around -30 MPa .^{50–52} As mentioned above, avoiding such tiny insoluble droplets is basically impossible. The other insight from Figure 4 is that once the droplet radius exceeds several tens of nanometers, any further increase in its size has a rather modest impact on the further decrease in the tensile strength.

Increasing the number of oil droplets in the system, N , has only a minor effect on the cavitation pressure. When cavitation is dominated by droplets, the rate simplifies to $k/N \approx k_{ow} + k_o$, indicating that cavitation pressure depends on N in the same weak manner as it does on observation time τ . For cavitation, the critical factor

remains the size of the largest oil droplet.

This observation underscores a challenging aspect of water purification: regardless of the extent of purification, preventing cavitation becomes a matter of eliminating the very last oil droplet in the system. Namely, that very last droplet is the “weakest link” and inevitably contributes to cavitation. Consequently, we assert that the cavitation pressures observed experimentally in aqueous systems reflect the presence of minute amounts of nonpolar residues, even in the most thoroughly purified samples.

Despite the points discussed above, nanoscopic oil droplets may be avoidable only in very small volumes of ultrapure water, specifically those approaching the micron scale. In a cubic micrometer of ultrapure water of a TOC purity level of 1 $\mu\text{g/L}$, the condensed organic content would amount to an oil droplet with a radius of one nanometer (equivalent to 50 decane molecules). However, since smaller organic molecules dissolve at this TOC, micrometer-sized water volumes may indeed realistically be free of organic aggregates larger than around 1 nm in size. This absence could elucidate the outcomes of experiments with microsized water inclusions in minerals, which have reported cavitation pressures as high as -140 MPa,^{18,29,30} aligning with our theoretical predictions for absolutely pure water of volume $V_w = 1 \mu\text{m}^3$ (red solid line in Fig. 1).

Finally, while our theoretical approach provides a foundational understanding of cavitation at nanoscopic hydrophobic inclusions, it has certain limitations. One of the limitations is the computational costs of MD simulations, which limit our ability to simulate much larger systems or extend them to longer time scales. Consequently, we have to rely on the integration with CNT, which has its own simplifications and shortcomings.^{57,58} For instance, we have used a simplified analytic expression for ΔG_{ow} , potentially contributing to the suboptimal fit in Figure 5c. Another limitation concerns the realism of our model. We assume no dissolved gases within the oil phase, while, in real scenarios, gases and gas pockets, especially in larger hydrophobic droplets, may influence cavitation dynamics and could introduce additional effects not captured here. For example, a recent study has shown that a sudden pressure drop in shockwave experiments can trigger the nucleation of gas bubbles from a locally supersaturated liquid with gas.⁵⁹

3. CONCLUSIONS

Even the most rigorously purified water samples contain insoluble aggregates and droplets. By integrating MD simulations with classical nucleation theory, we have quantitatively evaluated the impact of these tiny organic aggregates on cavitation pressure in water. Remarkably, a single nanoscopic oil droplet, merely a few nanometers across, can induce cavitation at pressure magnitudes substantially lower than those predicted for absolutely pure water. Specifically, we find that cavitation pressures drop to levels similar to those in bulk hydrocarbons, approximately -30 MPa, a value consistent with measurements from highly purified water experiments.

The quest for absolute water purity in any macroscopically significant system remains an elusive goal, suggesting that the theoretical tensile strength of water may be inherently unattainable in experimental contexts. However, an intriguing outlier exists in the form of microsized inclusions, which are so small that they could actually be free from clusters formed by impurities, enabling cavitation pressures as high as -140 MPa to be documented.^{18,29,30}

Understanding the role of hydrophobic inclusions provides valuable insights into xylem transport in plants, where hydrophobic and amphiphilic biomolecules, such as lipids, are present.⁶⁰ Although these molecules might initially seem like potential nucleation sites, they

appear to be unproblematic at pressures of -10 MPa found in plant xylem. We intend to investigate their specific role in future work.

Our findings extend beyond the realm of cavitation, shedding light on closely related processes such as the boiling of superheated water, bubble nucleation in supersaturated solutions, and even more general nucleation phenomena. The influence of tiny impurities on these processes highlights a broader principle: the profound impact that seemingly negligible components can have on the behavior of large-scale systems. This principle is of paramount importance, not only for advancing our theoretical understanding but also for improving experimental methodologies and technologies in fluid mechanics, material science, and beyond.

4. METHODS

4.1. Simulation details. Molecular dynamics simulations were conducted using Gromacs 2022.1,⁶¹ with an integration timestep of 2 fs. The temperature was maintained at 300 K using the v-rescale thermostat,⁶² except in cases where we deliberately examined temperature dependence. The pressure was controlled by the C-rescale barostat⁶³ with isotropic coupling. For simulating decane, we used the all-atom CHARMM36⁶⁴ force field. Electrostatic and Lennard-Jones (LJ) interactions were treated using particle mesh Ewald (PME)^{65,66} methods with a 1.4 nm real-space cutoff. Unlike traditional approaches that employ a cutoff for handling LJ interactions, we used PME summation of LJ interactions⁶⁷ with a real-space cutoff of 1.4 nm. This approach accurately reproduces experimental values of decane surface tensions over a range of temperatures, as tested recently.⁴⁹ We opted for the TIP4P/2005⁴² model for water, a 4-point model renowned for its accurate reproduction of experimental interfacial tensions and its compatibility with the CHARMM36 force field. As a comparison to the TIP4P/2005 model, we also tested the OPC⁴⁴ water model for bulk water simulations. While the OPC model effectively reproduces a comprehensive set of bulk properties, including the surface tension, very well,⁴⁴ it demonstrates less favorable results when combined with the CHARMM36 force field for alkanes.

4.2. Ramping pressure method. Evaluating the attempt frequency densities for cavitation (κ_w , κ_{ow} , and κ_o) via simulations at constant negative pressure by measuring the mean cavitation time turns out to be impractical. The primary difficulty lies in the very strong dependence of the cavitation time on the imposed pressure. There exists only a very narrow window of negative pressures where cavitation events can be observed within feasible simulation times, without overly reducing the free energy barrier. Predicting this optimal range of pressures in advance is difficult.

To circumvent these challenges, we employ the pressure ramp method,^{35,43} in which we impose a linearly increasing negative pressure over time, defined as $p(t) = \dot{p}t$, where \dot{p} is the rate of pressure change, assumed to be negative ($\dot{p} < 0$). Consequently, the free energy barrier decreases over time, reaching a threshold low enough to allow a cavitation event within the simulation time. This protocol renders reaction rates (such as k_w in eq 4) time-dependent. Solving the time-dependent transition rate equations for $k(t)$, as described in Ref. 35, brings us to the following equation

$$p_{\text{cav}}^* = \dot{p} \int_0^\infty e^{-k_0 I(t)} dt \quad (11)$$

where k_0 is the attempt frequency and

$$I(t) = \int_0^t e^{-\beta G^*(\tau)} d\tau \quad (12)$$

with $G^*(t)$ being the time-dependent free energy barrier as a direct consequence of $p(t)$. Equation 11 predicts the mean cavitation pressure, p_{cav}^* , in a system subjected to a pressure ramp at a rate of \dot{p} . This “dynamic” cavitation pressure p_{cav}^* should not be confused with the cavitation pressure, p_{cav} , observed under constant pressure conditions, which is our final aim to compute.

Since Gromacs does not support simulating a pressure ramp, we devised a workaround by conducting a sequence of short simulations. Each subsequent simulation was set to a pressure 0.1 MPa lower than its predecessor,

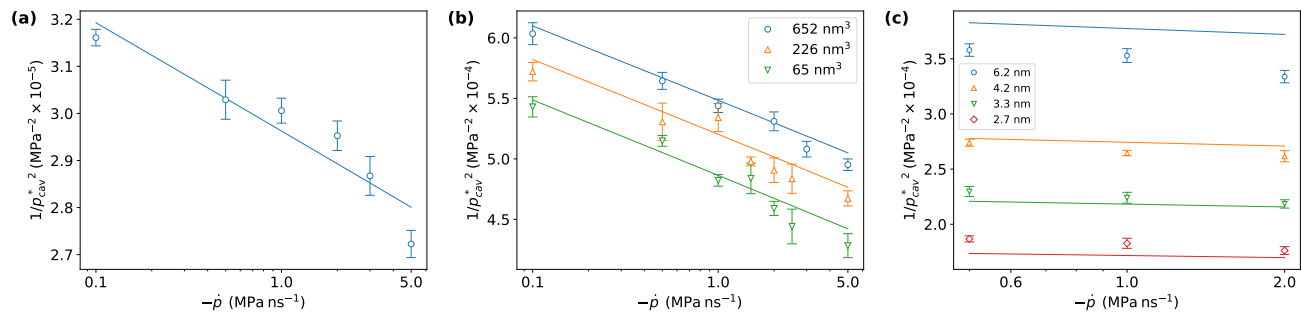


Figure 5: Mean dynamic cavitation pressures from pressure ramp simulations, plotted as $1/p_{cav}^{*2}$ against pressure rate for (a) bulk water with a volume of 731 nm^3 , (b) bulk decane of three different volumes (see legend), and (c) oil droplets with four different initial radii, R_o (see legend), in water. Solid lines are fits of eq 11 to the data points. In panel (a), the fit corresponds to the single volume, whereas in panels (b) and (c), global fits are simultaneously applied across all three and four datasets, respectively.

effectively emulating a linear pressure decrease. The duration of each simulation depends on the desired pressure rate \dot{p} . We identify a cavitation event based on an abrupt increase in the system’s volume after it had linearly risen due to the increasing negative pressure. We employed the random sample consensus (RANSAC)⁶⁸ algorithm to accurately pinpoint the moment when the volume begins to increase sharply. For each setup, we conducted 8 to 10 independent simulation runs to determine the mean dynamic cavitation pressure, p_{cav}^* , at specific rates of pressure change, \dot{p} . In doing so, we plot $1/p_{cav}^{*2}$ against $-\dot{p}$, as shown in Figure 5. Subsequently, we fit eq 11 (shown by lines) to the simulation data points with k_0 and the Tolman length (which enters the free energy barrier) as fitting parameters.

Specifically, for bulk water (Figure 5a), the attempt frequency k_0 is linked to the simulation volume V_w through the relation $k_0 = \kappa_w V_w$ from which κ_w is extracted. In the case of bulk decane (Figure 5b), the attempt frequency is $k_0 = \kappa_o V_o$, where V_o is the simulation volume. Given that we conducted simulations over three volumes in this case, we perform a global fit to all three datasets, with κ_o and δ_o as fitting parameters. Finally, for heterogeneous cavitation at the droplet interface (Figure 5c), the attempt frequency is connected to the droplet area as $k_0 = 4\pi\kappa_{ow}R_o^2$. With four different radii simulated, we again perform a global fit to all four datasets with κ_{ow} and δ_{eff} as the fitting parameters.

Table 1: Model parameters obtained from pressure ramp simulations that are used in CNT.

System	Parameter values
Cavitation in bulk water (w)	$\kappa_w = 1.25 \times 10^{18} \text{ s}^{-1} \text{ nm}^{-3}$ $\delta_w = -0.058 \text{ nm}$
Cavitation in bulk decane (o)	$\kappa_o = 5.4 \times 10^9 \text{ s}^{-1} \text{ nm}^{-3}$ $\delta_o = -0.116 \text{ nm}$
Cavitation at o/w interface	$\kappa_{ow} = 7.8 \times 10^{13} \text{ s}^{-1} \text{ nm}^{-2}$ $\delta_{eff} = -0.076 \text{ nm}$
Water–vapor	$\gamma_w = 68 \text{ mNm}^{-1}$
Decane–water	$\gamma_{ow} = 57 \text{ mNm}^{-1}$
Decane–vapor	$\gamma_o = 23 \text{ mNm}^{-1}$

Acknowledgments. We thank Fabio Staniscia for useful discussions. M.Š. and M.K. acknowledge financial support from the Slovenian Research and Innovation Agency ARIS (contracts P1-0055 and J1-4382).

Author contributions. **Marin Šako:** Investigation, Formal analysis, Software, Writing - Original Draft, Writing - Review & Editing, Visualization. **Roland R. Netz:** Conceptualization, Methodology, Writing - Review & Editing. **Matej Kanduč:** Conceptualization, Methodology, Writing - Review & Editing, Supervision, Project administration, Funding acquisition.

Data availability. Simulation files and Python scripts used to perform pressure-ramp simulations are available at <https://github.com/sajeta/pressure-ramp-md/tree/main>.

References

- (1) Caupin, F.; Herbert, E. Cavitation in water: a review. *C R Phys* **2006**, *7*, 1000–1017, Nucleation.
- (2) Stroock, A. D.; Pagay, V. V.; Zwieniecki, M. A.; Michele Holbrook, N. The physicochemical hydrodynamics of vascular plants. *Annu. Rev. Fluid Mech.* **2014**, *46*, 615–642.
- (3) Smith, A. M. Negative pressure generated by octopus suckers: a study of the tensile strength of water in nature. *J. Exp. Biol.* **1991**, *157*, 257–271.
- (4) Noblin, X.; Rojas, N.; Westbrook, J.; Llorens, C.; Argentina, M.; Dumais, J. The fern sporangium: a unique catapult. *Science* **2012**, *335*, 1322–1322.
- (5) Wheeler, T. D.; Stroock, A. D. The transpiration of water at negative pressures in a synthetic tree. *Nature* **2008**, *455*, 208–212.
- (6) Pagay, V.; Santiago, M.; Sessoms, D. A.; Huber, E. J.; Vincent, O.; Pharkya, A.; Corso, T. N.; Lakso, A. N.; Stroock, A. D. A microtensiometer capable of measuring water potentials below -10 MPa. *Lab Chip* **2014**, *14*, 2806–2817.
- (7) Vincent, O.; Sessoms, D. A.; Huber, E. J.; Guioth, J.; Stroock, A. D. Drying by cavitation and poroelastic relaxations in porous media with macroscopic pores connected by nanoscale throats. *Phys. Rev. Lett.* **2014**, *113*, 134501.
- (8) Dular, M.; Bachert, B.; Stoffel, B.; Širok, B. Relationship between cavitation structures and cavitation damage. *Wear* **2004**, *257*, 1176–1184.
- (9) Reuter, F.; Deiter, C.; Ohl, C.-D. Cavitation erosion by shockwave self-focusing of a single bubble. *Ultrason. Sonochem.* **2022**, *90*, 106131.
- (10) Adhikari, U.; Goliaei, A.; Berkowitz, M. L. Mechanism of membrane poration by shock wave induced nanobubble collapse: A molecular dynamics study. *J. Phys. Chem. B* **2015**, *119*, 6225–6234.
- (11) Peters, A.; Sagar, H.; Lantermann, U.; el Moctar, O. Numerical modelling and prediction of cavitation erosion. *Wear* **2015**, *338*, 189–201.
- (12) Coleman, A. J.; Saunders, J. E. A survey of the acoustic output of commercial extracorporeal shock wave lithotripters. *Ultrasound Med. Biol.* **1989**, *15*, 213–227.
- (13) Caupin, F. Escaping the no man’s land: Recent experiments on metastable liquid water. *J. Non-Cryst. Solids* **2015**, *407*, 441–448.
- (14) Debenedetti, P. G. *Metastable liquids: concepts and principles*; Princeton university press, 1996.
- (15) Fisher, J. C. The fracture of liquids. *J. Appl. Phys* **1948**, *19*, 1062–1067.
- (16) Caupin, F. Liquid-vapor interface, cavitation, and the phase diagram of water. *Phys. Rev. E* **2005**, *71*, 051605.
- (17) Caupin, F.; Stroock, A. D. The stability limit and other open questions on water at negative pressure. *Liquid Polymorphism* **2013**, *152*, 51–80.
- (18) Azouzi, M. E. M.; Ramboz, C.; Lenain, J.-F.; Caupin, F. A coherent

- picture of water at extreme negative pressure. *Nat. Phys.* **2013**, *9*, 38–41.
- (19) Menzl, G.; Gonzalez, M. A.; Geiger, P.; Caupin, F.; Abascal, J. L.; Valeriani, C.; Dellago, C. Molecular mechanism for cavitation in water under tension. *Proc. Natl. Acad. Sci. U.S.A.* **2016**, *113*, 13582–13587.
- (20) Wang, P.; Gao, W.; Wilkerson, J.; Liechti, K. M.; Huang, R. Cavitation of water by volume-controlled stretching. *Extreme Mech. Lett.* **2017**, *11*, 59–67.
- (21) Xie, H.; Xu, Y.; Zhong, C. A study of cavitation nucleation in pure water using molecular dynamics simulation. *Chin. Phys. B* **2022**, *31*, 114701.
- (22) P Lamas, C.; Vega, C.; G Noya, E.; Sanz, E. The water cavitation line as predicted by the TIP4P/2005 model. *J. Chem. Phys.* **2023**, *158*.
- (23) Harvey, E. N.; Barnes, D.; McElroy, W. D.; Whiteley, A. H.; Pease, D.; Cooper, K. Bubble formation in animals. I. Physical factors. *J. Cell. Comp. Physiol.* **1944**, *24*, 1–22.
- (24) Atchley, A. A.; Prosperetti, A. The crevice model of bubble nucleation. *J. Acoust. Soc. Am.* **1989**, *86*, 1065–1084.
- (25) Jones, S.; Evans, G.; Galvin, K. Bubble nucleation from gas cavities—a review. *Adv. Colloid Interface Sci.* **1999**, *80*, 27–50.
- (26) Borkent, B. M.; Gekle, S.; Prosperetti, A.; Lohse, D. Nucleation threshold and deactivation mechanisms of nanoscopic cavitation nuclei. *Phys. Fluids* **2009**, *21*.
- (27) Gao, Z.; Wu, W.; Wang, B. The effects of nanoscale nuclei on cavitation. *J. Fluid Mech.* **2021**, *911*, A20.
- (28) Lauterborn, W.; Mettin, R. In *Power Ultrasonics (Second Edition)*, second edition ed.; Gallego-Juárez, J. A., Graff, K. F., Lucas, M., Eds.; Woodhead Publishing Series in Electronic and Optical Materials; Woodhead Publishing, 2023; pp 23–52.
- (29) Zheng, Q.; Durben, D.; Wolf, G.; Angell, C. Liquids at large negative pressures: water at the homogeneous nucleation limit. *Science* **1991**, *254*, 829–832.
- (30) Alvarenga, A.; Grimdsitch, M.; Bodnar, R. Elastic properties of water under negative pressures. *J. Chem. Phys.* **1993**, *98*, 8392–8396.
- (31) Roger, K.; Cabane, B. Why are hydrophobic/water interfaces negatively charged? *Angew. Chem., Int. Ed. Engl.* **2012**, *51*, 5625.
- (32) Maali, A.; Boisgard, R.; Chraïbi, H.; Zhang, Z.; Kellay, H.; Würger, A. Viscoelastic drag forces and crossover from no-slip to slip boundary conditions for flow near air-water interfaces. *Phys. Rev. Lett.* **2017**, *118*, 084501.
- (33) Zhang, X.; Yang, Y.; Ngo, H. H.; Guo, W.; Wen, H.; Wang, X.; Zhang, J.; Long, T. A critical review on challenges and trend of ultra-pure water production process. *Sci. Total Environ.* **2021**, *785*, 147254.
- (34) Li, B.; Gu, Y.; Chen, M. Cavitation inception of water with solid nanoparticles: A molecular dynamics study. *Ultrason. Sonochem.* **2019**, *51*, 120–128.
- (35) Kanduč, M.; Schneck, E.; Loche, P.; Jansen, S.; Schenk, H. J.; Netz, R. R. Cavitation in lipid bilayers poses strict negative pressure stability limit in biological liquids. *Proc. Natl. Acad. Sci. U.S.A.* **2020**, *117*, 10733–10739.
- (36) Tolman, R. C. The effect of droplet size on surface tension. *J. Chem. Phys.* **1949**, *17*, 333–337.
- (37) Hänggi, P.; Talkner, P.; Borkovec, M. Reaction-rate theory: fifty years after Kramers. *Rev. Mod. Phys.* **1990**, *62*, 251.
- (38) Herbert, E.; Balibar, S.; Caupin, F. Cavitation pressure in water. *Phys. Rev. E* **2006**, *74*, 041603.
- (39) Blander, M.; Katz, J. L. Bubble nucleation in liquids. *AIChE J.* **1975**, *21*, 833–848.
- (40) Pettersen, M.; Balibar, S.; Maris, H. Experimental investigation of cavitation in superfluid He4. *Phys. Rev. B* **1994**, *49*, 12062.
- (41) Allen, R. J.; Valeriani, C.; Ten Wolde, P. R. Forward flux sampling for rare event simulations. *J. Phys.: Condens. Matter* **2009**, *21*, 463102.
- (42) Abascal, J. L. F.; Vega, C. A general purpose model for the condensed phases of water: TIP4P/2005. *J. Chem. Phys.* **2005**, *123*, 234505.
- (43) Boucher, P.-A.; Joós, B.; Zuckermann, M. J.; Fournier, L. Pore formation in a lipid bilayer under a tension ramp: modeling the distribution of rupture tensions. *Biophys. J.* **2007**, *92*, 4344–4355.
- (44) Izadi, S.; Anandakrishnan, R.; Onufriev, A. V. Building Water Models: A Different Approach. *J. Phys. Chem. Lett.* **2014**, *5*, 3863–3871, PMID: 25400877.
- (45) Uematsu, Y.; Bonthuis, D. J.; Netz, R. R. Impurity effects at hydrophobic surfaces. *Curr. Opin. Electrochem.* **2019**, *13*, 166–173.
- (46) Serravalle, S.; Pisano, M.; Sciacca, M. F.; Salamone, N.; Sicali, L.; Mazzara, G.; Costa, L.; La Rosa, C. Critical micellar concentration determination of pure phospholipids and lipid-raft and their mixtures with cholesterol. *Proteins Struct. Funct. Bioinforma.* **2024**.
- (47) Letinski, D. J.; Parkerton, T. F.; Redman, A. D.; Connelly, M. J.; Peterson, B. Water solubility of selected C9–C18 alkanes using a slow-stir technique: Comparison to structure–property models. *Chemosphere* **2016**, *150*, 416–423.
- (48) Berkelaar, R. P.; Dietrich, E.; Kip, G. A.; Kooij, E. S.; Zandvliet, H. J.; Lohse, D. Exposing nanobubble-like objects to a degassed environment. *Soft Matter* **2014**, *10*, 4947–4955.
- (49) Šako, M.; Staniscia, F.; Schneck, E.; Netz, R. R.; Kanduč, M. Conditions for the stable adsorption of lipid monolayers to solid surfaces. *PNAS Nexus* **2023**, *2*, pgad190.
- (50) Galloway, W. J. An experimental study of acoustically induced cavitation in liquids. *J. Acoust. Soc. Am.* **1954**, *26*, 849–857.
- (51) Apfel, R. E.; Smith, M. P. The tensile strength of di-ethyl ether using Briggs’s method. *J. Appl. Phys.* **1977**, *48*, 2077–2078.
- (52) Ohde, Y.; Watanabe, H.; Hiro, K.; Motoshita, K.; Tanzawa, Y. Raising of negative pressure to around-200 bar for some organic liquids in a metal Berthelot tube. *J. Phys. D Appl. Phys.* **1993**, *26*, 1188.
- (53) Vinogradov, V. E.; Pavlov, P. A. The boundary of limiting superheats of n-heptane, ethanol, benzene, and toluene in the region of negative pressures. *High Temp.* **2000**, *38*, 379–383.
- (54) Bormashenko, E. Why are the values of the surface tension of most organic liquids similar? *Am. J. Phys.* **2010**, *78*, 1309–1311.
- (55) Binyaminov, H.; Abdullah, F.; Zargarzadeh, L.; Elliott, J. A. Thermodynamic Investigation of Droplet–Droplet and Bubble–Droplet Equilibrium in an Immiscible Medium. *J. Phys. Chem. B.* **2021**, *125*, 8636–8651.
- (56) Makkonen, L.; Kurkela, J. Another look at the interfacial interaction parameter. *J. Colloid Interface Sci.* **2018**, *529*, 243–246.
- (57) Erdemir, D.; Lee, A. Y.; Myerson, A. S. Nucleation of crystals from solution: classical and two-step models. *Acc. Chem. Res.* **2009**, *42*, 621–629.
- (58) Karthika, S.; Radhakrishnan, T.; Kalaichelvi, P. A review of classical and nonclassical nucleation theories. *Cryst. Growth Des.* **2016**, *16*, 6663–6681.
- (59) Pfeiffer, P.; Shahrooz, M.; Tortora, M.; Casciola, C. M.; Holman, R.; Salomir, R.; Meloni, S.; Ohl, C.-D. Heterogeneous cavitation from atomically smooth liquid–liquid interfaces. *Nat. Phys.* **2022**, *18*, 1431–1435.
- (60) Schenk, H. J.; Steppe, K.; Jansen, S. Nanobubbles: a new paradigm for air-seeding in xylem. *Trends Plant Sci.* **2015**, *20*, 199–205.
- (61) Bekker, H.; Berendsen, H.; Dijkstra, E.; Achterop, S.; Vondrumen, R. v.; Vanderspoel, D.; Sijbers, A.; Keegstra, H.; Renardus, M. Gromacs—a parallel computer for molecular-dynamics simulations. 4th international conference on computational physics (PC 92). 1993; pp 252–256.
- (62) Bussi, G.; Donadio, D.; Parrinello, M. Canonical sampling through velocity rescaling. *J. Chem. Phys.* **2007**, *126*, 014101.
- (63) Bernetti, M.; Bussi, G. Pressure control using stochastic cell rescaling. *J. Chem. Phys.* **2020**, *153*, 114107.
- (64) Vanommeslaeghe, K.; Hatcher, E.; Acharya, C.; Kundu, S.; Zhong, S.; Shim, J.; Darian, E.; Guvench, O.; Lopes, P.; Vorobyov, I.; Mackerell, A. CHARMM general force field: A force field for drug-like molecules compatible with the CHARMM all-atom additive biological force fields. *J. Comput. Chem.* **2010**, *31*, 671–690.
- (65) Darden, T.; York, D.; Pedersen, L. Particle Mesh Ewald: An N log(N) Method for Ewald Sums in Large Systems. *J. Chem. Phys.* **1993**, *98*, 10089–10092.
- (66) Essmann, U.; Perera, L.; Berkowitz, M. L.; Darden, T.; Lee, H.; Pedersen, L. G. A Smooth Particle Mesh Ewald Method. *J. Chem. Phys.* **1995**, *103*, 8577–8593.
- (67) Wennberg, C. L.; Murtola, T.; Hess, B.; Lindahl, E. Lennard-Jones lattice summation in bilayer simulations has critical effects on surface tension and lipid properties. *J. Chem. Theory Comput.* **2013**, *9*, 3527–3537.
- (68) Fischler, M. A.; Bolles, R. C. Random Sample Consensus: A Paradigm for Model Fitting with Applications to Image Analysis and Automated Cartography. *Commun. ACM* **1981**, *24*, 381–395.